Nonlinear dynamics of two-dimensional undercompressive shocks

Mark Bowen [a] Jeanman Sur [b] Andrea L. Bertozzi [c,b]
Robert P. Behringer [b]

[a] *School of Mathematical Sciences, University of Nottingham, University Park, Nottingham NG7 2RD, UK*

[b] *Department of Physics and Center for Nonlinear and Complex Systems, Duke University, Durham, NC 27708, USA*

[c] *Department of Mathematics, Duke University, Durham, NC 27708 and Univ. of California Los Angeles, Box 951555, Los Angeles, CA 90095-1555, USA*

Abstract

We consider the problem of a thin film driven by a thermal gradient with an opposing gravitational force. Under appropriate conditions, an advancing film front develops a leading undercompressive shock followed by a trailing compressive shock. Here, we investigate the nonlinear dynamics of these shock structures that describe a surprisingly stable advancing front. We compare two dimensional simulations with linear stability theory, shock theory, and experimental results. The theory/experiment considers the propagation of information through the undercompressive shock towards the trailing compressive shock. We show that a local perturbation interacting with the undercompressive shock leads to nonlocal effects at the compressive shock.

Key words:
Thin films, shocks, undercompressive shocks, Marangoni effect
PACS: 68.15.+e

1 Introduction

When a liquid film is driven by a body force, such as gravity on an inclined plane [1], or by a Marangoni surface stress as imposed by a temperature gradient [2], the steep leading edge of the film typically evolves into fingers. Mathematically, the rapid variation in height at the front of the film corresponds to the presence of a smoothed compressive shock; the region around the shock is often referred to as the capillary ridge. A standard linear stability analysis shows the shock to be unstable to large wavelength

perturbations [3,4]. It is this instability that leads to the fingering phenomena seen in experiments. Detailed numerical simulations (see, for example, [5] and [6] and references therein) support this theory. More complex dynamics can arise in experimental systems when a thin film is jointly driven by a surface stress and a comparable body force. In the experiments of [7] a large capillary ridge developed, but the moving front of the film remained surprisingly stable and fingering phenomena did not occur.

A one-dimensional theory was first put forward for the observed experimental results in [8] and [9]. Here, it was shown that, in general, solutions to a model evolution equation typically evolve into either (1) a single compressive shock, (2) a separating double shock structure involving a leading undercompressive wave and trailing compressive wave, or (3) a rarefaction-undercompressive shock structure. Recently, a new structure involving an undercompressive and reverse undercompressive shock was also identified in [10] and [11]. Case (1) is generic when there is a single driving force acting on the thin film (as described above). We shall focus on cases (1) and (2) so that we can make a comparison between the well understood dynamics of case (1) versus the time evolving dynamics of case (2). The leading undercompressive shock in case (2) is stable to perturbations (an issue we explore in detail later) and is the reason why, in the experiments of [8], the film front resists the fingering instability. This provides an interesting mechanism to produce uniform coating flows.

We compare (to the best of our knowledge, for the first time) experimental results featuring undercompressive-compressive shock pairs with fully two dimensional numerical simulations and show that large scale patterns can be predicted by a combination of linear theory and shock dynamics, including transport along characteristics. We also show how to extend the stability analysis for a single compressive shock to dynamically evolving base states featuring multiple nonlinear structures (in this case undercompressive-compressive shock pairs). We note that a standard stability analysis fails not just because the base state is time dependent and features multiple shocks, but because the interaction of the shocks with perturbations cannot be investigated completely independently for each shock; experimental evidence and numerical simulations indicate that perturbations impinging onto the leading undercompressive shock are partially transferred to the trailing compressive shock and consequently the dynamics are not localised to either shock. The methodology can be easily developed to handle more complex problems involving various spatial structures and timescales.

2 Mathematical model and background

We model the dynamics of a thin liquid film on an inclined substrate, driven by the combined effects of a thermally induced Marangoni force and gravity. By application of a lubrication approximation (see [9,8] and references therein for more details) we arrive

at the evolution equation

$$\frac{\partial u}{\partial t}+\frac{\partial}{\partial x}\left(\frac{\tau u^2}{2\eta}-\frac{\rho g u^3\sin\alpha}{3\eta}\right)=-\nabla\cdot\left[\left(\frac{\gamma u^3\nabla\Delta u}{3\eta}\right)-\left(\frac{\rho g u^3\cos\alpha}{3\eta}\nabla u\right)\right]. \tag{2.1}$$

The film height u is a function of position along the incline x and of the transverse variable y as well as of time, t. The parameters are α (angle of inclination of the substrate from the horizontal), ρ (density), g (gravity), η (viscosity), τ (temperature gradient) and γ (surface tension). We rescale to dimensionless units: $u=H\hat{u}$, $x=l\hat{x}$, $t=T\hat{t}$, where $H=3\tau/2\rho g\sin\alpha$, $l=\left(3\gamma\tau/2\rho^2 g^2\sin^2\alpha\right)^{1/3}$, and $T=(2\eta/\tau^2)\left(4\tau\gamma\rho g\sin\alpha/9\right)^{1/3}$. This leads to (dropping the hats for ease of notation) the nondimensionalised equation

$$\frac{\partial u}{\partial t}+\frac{\partial}{\partial x}[f(u)]=-\nabla\cdot(u^3\nabla\Delta u)+D\nabla\cdot(u^3\nabla u) \tag{2.2}$$

where $D=(9\tau^2/4\gamma\rho g)^{1/3}\cot\alpha/(\sin\alpha)^{1/3}$ and $f(u)=u^2-u^3$. For typical experiments, $D\ll 1$, and we simplify the model by setting $D=0$,

$$\frac{\partial u}{\partial t}+\frac{\partial}{\partial x}[f(u)]=-\nabla\cdot(u^3\nabla\Delta u); \tag{2.3}$$

a complete investigation for the one-dimensional problem of the role of the second order diffusive term in (2.2) in terms of the size of D can be found in [12]. Equation (2.3) is also coupled to the far-field conditions

$$u\to u_- \qquad \text{as} \qquad x\to-\infty, \quad u\to u_+ \qquad \text{as} \qquad x\to+\infty \tag{2.4}$$

representing a precursor film of thickness u_+ ahead of the front [8] and a trailing flat film with thickness u_- [13]. Symmetry boundary conditions are applied in the y-direction. We also take single-step initial data consistent with the boundary conditions (2.4), namely

$$u(x,y,0)=u_0(x)=\begin{cases}u_- & \text{for} \quad x<x_0\\ u_+ & \text{for} \quad x\geq x_0\end{cases} \tag{2.5}$$

for some fixed x_0.

On large length and time scales, the fourth order diffusive term in (2.3) (representing surface tension effects) is negligible and the consequent dynamics of the solution are given by the reduced quasilinear scalar hyperbolic equation on the left hand side of (2.3), namely

$$\frac{\partial u}{\partial t}+\frac{\partial}{\partial x}[f(u)]=0. \tag{2.6}$$

The overall dynamics of the solutions are therefore controlled by the competing convective fluxes due to gravity and the Marangoni stress. In the absence of the diffusion term, equation (2.6) may be tackled by application of characteristic methods (see [14]). Characteristics are, for this problem, straight lines in (x,t) space along which the solution to (2.6) remains constant. A simple calculation shows that the slope of each of the characteristics is $dt/dx = 1/(2u_0 - 3u_0^2)$ where u_0 is given by (2.5) for each value of x at $t = 0$. Locally, therefore, information is transferred with a characteristic speed given by

$$F(u_0) = 2u_0 - 3u_0^2 \tag{2.7}$$

where u_0 takes the constant value u_- for $x < x_0$ and similarly $u_0 = u_+$ for $x > x_0$. If u_+ and u_- are chosen so that $F(u_-) > F(u_+)$, the discontinuity in the initial data at $x = x_0$ is preserved and moves to the right with a finite speed s; propagating discontinuities in the solution to (2.6) are typically termed shocks. At the shock, the characteristic formula given above is not valid and is replaced by the Rankine-Hugoniot jump condition which gives s in terms of the change in height across the shock (see (2.10)). Shocks in the solution of (2.6) represent rapidly changing height profiles in the experiments; smoothing of the shocks occurs due to the fourth order diffusive term on the right-hand side of (2.3) which becomes important when large gradients arise in the solution.

Unperturbed solutions of (2.3) are plane wave solutions independent of y. We consider a travelling wave solution $u = \hat{u}(x - st)$. Transforming to a moving reference frame, with speed s and adjusted flux function

$$f(\hat{u}) = \hat{u}^2 - \hat{u}^3 - s\hat{u}, \tag{2.8}$$

leads to the condition that $\hat{u}$ satisfies

$$[f(\hat{u})]_x + (\hat{u}^3\hat{u}_{xxx})_x = 0. \tag{2.9}$$

Equation (2.9) is immediately integrable, the constant of integration being specified by the far-field conditions (2.4). For a single shock (as in case (1)) this gives the standard Rankine-Hugoniot condition for the speed

$$s = \frac{f(u_+) - f(u_-)}{(u_+ - u_-)} = \frac{u_+^2 - u_+^3 - (u_-^2 - u_-^3)}{(u_+ - u_-)}. \tag{2.10}$$

Choosing s from (2.10) for the travelling wave speed therefore leads to a single shock profile that appears to be fixed in space. Strictly speaking, however, we have to be careful with our choice of s for case (2) as, in general, it will take different values for the compressive and undercompressive shocks. This explains (as discussed in the introduction) why the separation between the undercompressive and compressive shocks changes with time.

If the speed of the shock satisfies the entropy condition $F(u_-) > s > F(u_+)$ (alternatively, in a moving reference frame, $f'(u_-) > 0 > f'(u_+)$), the shock is said to be compressive. An example of a compressive shock solution for (2.3) is illustrated in Figure 1 (left) along with the corresponding characteristic diagram given as Figure 1 (right). A compressive shock has characteristics which enter on both sides suggesting a loss of information into the shock from the surrounding medium. The initial data (2.5) was fixed by choosing $u_+ = 0.1$, $u_- = 0.3321$ and $x_0 = 500$; we explain the choice of u_- below. The one-dimensional version of equation (2.3) was then integrated forward in time (in a moving reference frame of speed s given by (2.10)) until the shock profile formed. Also shown in Figure 1 (left) is the motion of a Gaussian perturbation, $\exp(-(x - x_p)^2)$, imposed on the solution (in the translating reference frame the shock appears fixed with the perturbation moving). Figure 1 (left) contains two sets of numerical data, one for a perturbation initially placed at $x_p = 450$ and the other set of results for $x_p = 590$; the numerical methodology is discussed in Section 5.

Non-classical undercompressive shocks, which do not satisfy $F(u_-) > s > F(u_+)$, can also occur in the solution of (2.3). The undercompressive shocks, which we consider here, satisfy the supersonic speed relationship $s > F(u_-) > F(u_+)$ (which corresponds to $0 > f'(u_-) > f'(u_+)$). Figure 2 (left) shows a solution to (2.3) featuring an undercompressive shock. Here, $u_+ = 0.1$, $u_- = 0.5679$ and $x_0 = 500$ in (2.5), and we again work in a moving reference frame such that the shock appears fixed in space). It is noteworthy that only the value of u_- has been changed from the compressive shock simulation shown in Figure 1 (left). For an undercompressive shock, information propagates into the shock on one side and escapes on the other (as shown in Figure 2 (right)). This does not imply, however, that information simply passes through unhindered. In fact, as later numerical simulations of transient behaviour illustrate (see Figure 8 (left)), the transition of a perturbation through an undercompressive shock is definitely not a simple transport process. As for the compressive shock simulation shown in Figure 1 (left), a perturbation is applied to the solution in Figure 2 (left). The perturbation is initially located at $x_p = 590$ for the results shown on the right of the undercompressive shock and at $x_p = 480$ for the results shown on the left. The characteristic diagram, Figure 2 (right), should be contrasted with the analogous schematic (Figure 1 (right)) for a compressive shock. It is important to note that in both the compressive and undercompressive shock simulations, the perturbation is carried in the direction of the characteristics. This phenomena will play a fundamental role in understanding the observed experimental results investigated throughout the rest of this paper.

We also note that the values of u_- chosen for the compressive and undercompressive shocks shown in Figure 1 (left) and Figure 2 (left) respectively, have not been chosen arbitrarily. A single undercompressive shock, can only be found, for $u_+ = 0.1$, when $u_- = 0.5679$, and the value of $u_- = 0.3321$ for the compressive shock was chosen so that

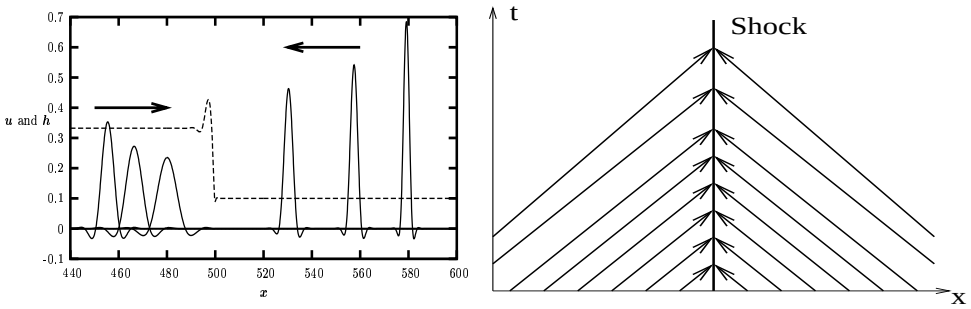

Fig. 1. The movement of perturbations for a compressive shock. We work in a moving reference frame in which the shock is stationary. (left) Numerical illustration of the movement of a perturbation with wavenumber $k = 0.25$. Arrows indicate the direction of increasing time (the perturbation on both sides of the shock is shown at times $t = 100, 300, 550$). (right) Schematic for the characteristics of a compressive shock.

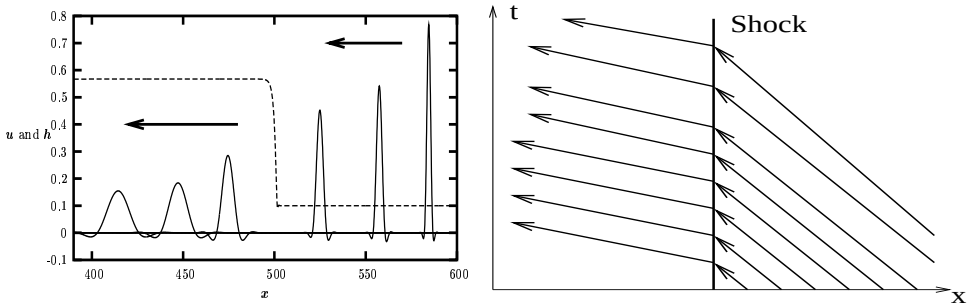

Fig. 2. The movement of perturbations for an undercompressive shock. The notation is as used in Figure 1. We work in a moving reference frame in which the shock is stationary. (left) Numerical illustration of the movement of a perturbation with wavenumber $k = 0.25$. Arrows indicate the direction of increasing time (the perturbation on both sides of the shock is shown at times $t = 50, 300, 600$). (right) Schematic for the characteristics of an undercompressive shock.

it travels with the same speed as the undercompressive shock (see [15]).

3 Description of experiments

The experiments are carried out with silicone oil (PDMS, viscosity, 100 cSt; surface tension, 0.0209 N.m at 25^oC) on a Silicon wafer. As sketched in Fig. 3, the wafer is clamped mechanically and thermally to a thin brass plate, across which we apply a uniform and temporally constant temperature gradient. We monitor this gradient by means of a series of thermistors embedded in the brass plate. We create the temperature gradient by means a resistive heater at the hot end, and a circulating water bath at the cold end. At the hot end, there is a bath of silicone oil. The meniscus emanating from this bath is located just above the lower end of the region of uniform temperature gradient. The film motion is then controlled by competing effects due to gravity and to the surface tension gradient, which has a typical value of 0.11 Pa. The substrate angle α is one of the

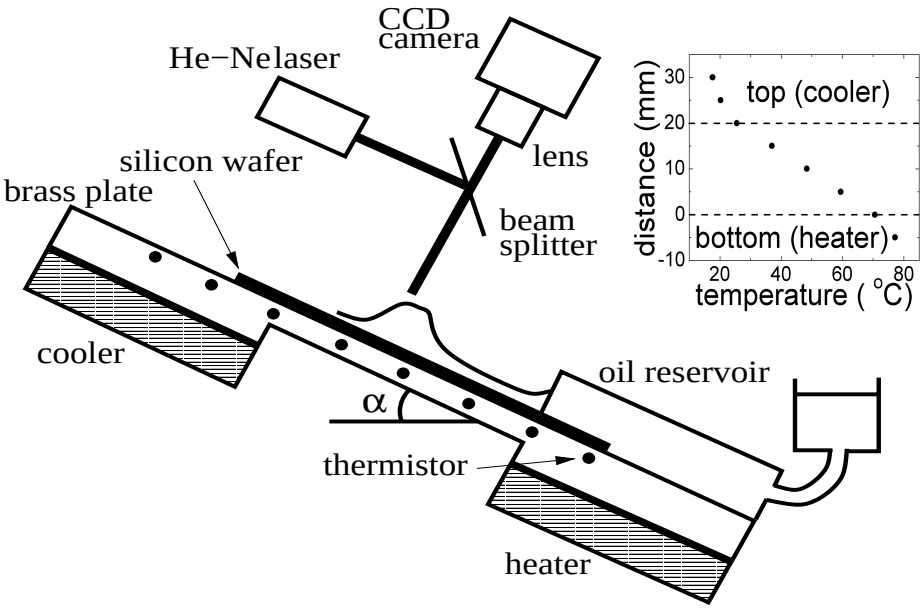

Fig. 3. Sketch of experimental apparatus. A thin film of silicon oil moves on an optically flat Silicon wafer along which there is a temperature gradient. This gradient drives a thin film against gravity through Marangoni forces. The temperature gradient is established along an underlying brass surface that lies between a lower heated reservoir of oil, and an upper brass block that is temperature-controlled by means of a water bath. We visualise the film profile interferometrically, as indicated. An additional IR laser can be applied to the surface in order to generate local heating.

key control parameters. As α increases, the effect of gravity is stronger, and the mean film height decreases.

We visualise the film thickness interferometrically. The film/substrate is illuminated by He-Ne laser light ($\lambda = 632.8$nm) that passes through a beam-expander/collimator, and reflects from a beam splitter. It then passes through the film, reflects from the polished Silicon substrate, and arrives at a CCD camera via the beam splitter. Images are then recorded digitally by a framegrabber. Each of these images shows a series of light and dark fringes, such that the difference between fringes corresponds to 0.225μm.

The last component of the apparatus that is relevant here involves a second 100mW IR laser. By directing the beam from this laser on the substrate, we can locally thin the film to effectively zero height. This provides a convenient way of generating local perturbations, and it also allows us to obtain an absolute determination of the film thickness (by counting the number of fringes between the bare spot and a point of interest). We can also sweep the beam across the substrate to generate perturbations of a well defined wavelength. Results using this technique will be reported elsewhere [16].

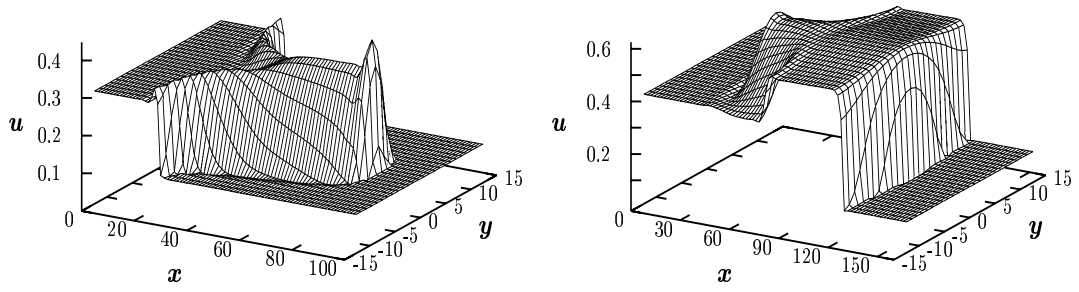

Fig. 4. The initial data is a jump discontinuity from u_- to $u_+ = 0.1$. (left) For $u_- = 0.3$, a compressive shock forms that is unstable to fingering. (right) For $u_- = 0.4$, an shock pair with a leading undercompressive and trailing compressive wave forms. The perturbation does not affect the leading wave.

4 Two-dimensional perturbations of shock structures

Previous analytical and numerical studies have focussed on the one-dimensional form of equation (2.3) (ignoring variations in y). However, the interaction of a moving front with a transverse perturbation is clearly a multi-dimensional phenomena and so one-dimensional studies alone do not explain the overall dynamics. Therefore, in this section, we introduce fully nonlinear two-dimensional simulations and make direct comparisons with experimental results. The simulations use an alternating direction implicit (ADI) method as discussed, for example, in [17] and [18]. Such a comparison, in which the numerics captures the full nonlinear dynamics in two dimensions, has not been considered before. These comparisons indicate that the model (2.3), starting from the initial data (2.5), is capable of accurately reproducing the complex structures seen in the experiments. This is followed, in Section 5, with a detailed linear stability analysis of the evolving double-shock structures.

We begin by considering the initial condition (2.5). This is consistent with the experimental procedure, as the existence of a precursor meniscus naturally leads to a step-like structure forming at the beginning of the experiments. We take $u_+ = 0.1$ and to contrast cases (1) and (2) we consider two different values of u_-, namely 0.3 and 0.4. Equation (2.3) is then integrated forward in time until the two-dimensional (although independent of y) shock structures form. In case (1) (corresponding to $u_- = 0.3$), a single compressive shock forms, while for case (2) (with $u_- = 0.4$) a double shock structure, comprised of a leading undercompressive shock and trailing compressive shock appears in the solution; this is consistent with the one-dimensional analytical study of [9].

We then impose a transverse perturbation with wavenumber $k = 0.24$ (cf. (5.11)) at the contact line, and track the ensuing dynamics. In case (1), the perturbation results in a classical fingering instability as shown in Figure 4 (left) which resembles the corresponding experimental flow, as shown in Figure 5 (top). In case (2), the leading front is

stable to transverse perturbations as shown in Figure 4 (right) and Figure 5 (bottom). We study this issue in detail in Section 5.

An important item of note in Figure 4 (right) is that although the perturbation initially interacts with the leading undercompressive shock, at later times the effect of the perturbation is present at both the undercompressive and trailing compressive shock. This suggests, for double-shock structures, that the perturbation is not localised to the leading front. This phenomena can be understood in terms of characteristics as introduced in Section 2. As indicated in Figure 2, a perturbation placed ahead of the leading undercompressive shock is swept along characteristics towards the front. Once the perturbation impinges onto the undercompressive shock, the characteristics emanating from behind the shock allow transfer of some of the perturbation towards the trailing compressive shock. The compressive shock, as illustrated in Figure 1 has characteristics that enter on both sides and so the escaping perturbation becomes blocked by the shock and cannot pass behind it. The overall effect is that the perturbation appears at both shocks as well as connecting between them. As the interaction of the perturbation with the undercompressive shock effects the behaviour of the perturbation at the trailing compressive shock, the linear stability analysis of the double shock structure cannot be performed by studying each shock independently . We discuss this issue further in Section 5 where we develop a 'dynamic' linear stability analysis of the double-shock structures.

Analysis [19] of the trailing shock in Figure 4 (right) shows it to be linearly unstable for disturbances with wavenumbers less than $k_c \approx 0.17$. It is noteworthy, that although we impose a $k = 0.24$ wavenumber disturbance for which the trailing shock should be stable, we initially gain a 'backward-finger' as seen in Figure 4 (right). However, for larger times, the finger decays in length and eventually vanishes. The early fingering dynamics are a consequence of nonlinearities being excited by the perturbation which is initially amplified by the compressive shock (see Section 5).

A perturbation can, in fact, be imposed experimentally at any location on the film surface by shining an infrared (IR) laser spot (wavelength 830 nm, 100 mW) onto the film. The laser spot heats the liquid film locally and induces a local Marangoni flow. The film profile is visualised by an interferometric method, as discussed above, and each interference fringe represents a different thickness (one fringe = 0.226 μm)[10]. Figure 6 shows an example of the resulting film flow due to the combination of local heating and the uniform surface tension gradient (top - experimental results, bottom - numerical results). In order to produce the numerical results seen in Figure 6 (bottom), we modify equation (2.3) by the introduction of the additional terms

$$2\sigma \left\{ \frac{\partial}{\partial x} \left((x - x_c) e^{-[(x-x_c)^2 + (y-y_c)^2]} u^2 \right) + \frac{\partial}{\partial y} \left((y - y_c) e^{-[(x-x_c)^2 + (y-y_c)^2]} u^2 \right) \right\}$$

to represent the local surface tension gradient induced by the laser spot. We start with initial data (2.5) ($u_- = 0.3$, $u_+ = 0.01$, $x_0 = 55$). After letting the double-shock form,

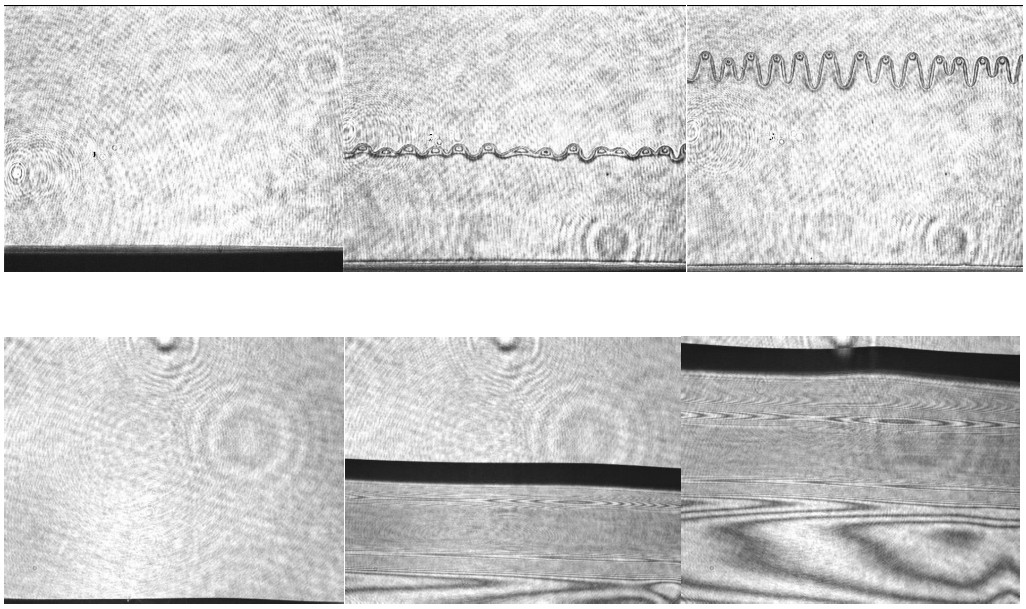

Fig. 5. Experimental results showing the two kinds of nonlinear structures that evolve. (top) A compressive wave that is unstable to fingering as in Figure 4 (left), (bottom) an undercompressive-compressive shock pair that appears to be stable as in Figure 4 (right).

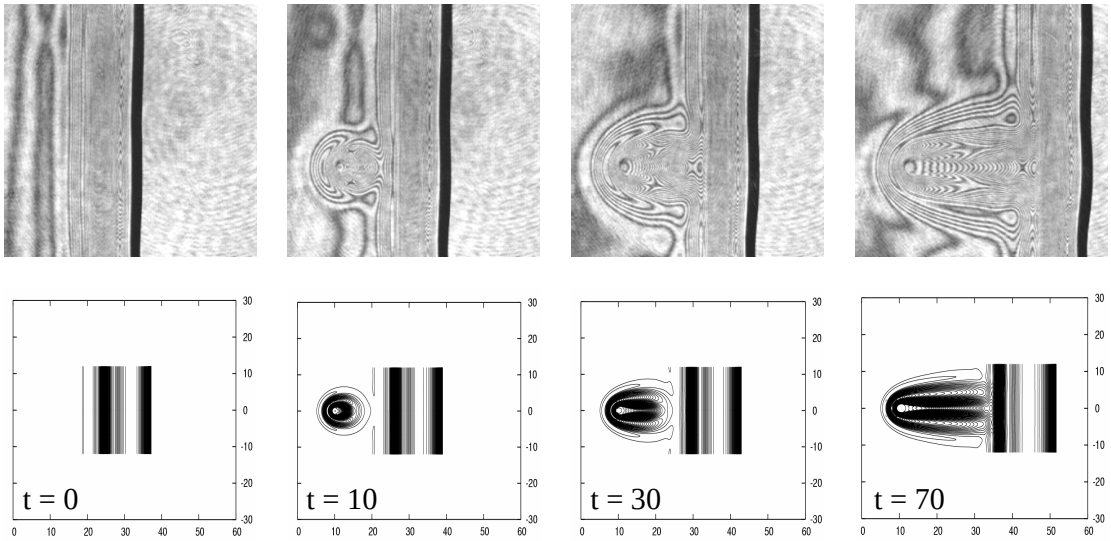

Fig. 6. (top) Experimental observation of a perturbation travelling into a trailing compressive shock. (bottom) Contour plots of two-dimensional numerical results which simulate the experiment in Figure 6 (top). The times indicated on the numerical results corresponds to the time after the double shock structure formed.

we 'turn on' the laser spot behind the bump ($x_c = 10$, $y_c = 0$) at $t = 600$ by setting $\sigma = 1.8$; before this time σ is taken to be zero. Even though the parameters are not exactly numerically matched with the experimental parameters, the numerical results are sufficient to illustrate that the qualitative behaviour is consistent with the experiments.

5 Dynamic linear stability and characteristic phenomena

We now present a dynamic linear stability theory for the one-dimensional shock structures by perturbing around a base state that evolves in time. The dynamic theory allows us to study stability of developing shocks and multiple shock solutions. Analysis of similar problems in thin film flow has been undertaken by [20] and [21], but to our knowledge, this is the first study to investigate the stability of solutions featuring multiple shock profiles that develop with time. We begin by reviewing the theory in [19] for the linear stability of single travelling waves (either compressive or undercompressive). This theory shows that, although compressive shocks lead to eigenfunctions with localised structure, the eigenfunctions for undercompressive shocks have a non-local structure. This has important consequences in understanding the dynamics of perturbations interacting with undercompressive-compressive shock pairs, as observed in experiments and numerical computations. In particular, we show that the non-localised eigenfunction for the undercompressive shock allows transport of information away from the shock (this is consistent with the characteristic diagram, Figure 2 (right)). Consider the solution ansatz

$$u(x,y,t) = \bar{u}(x,t) + \varepsilon h(x,t)\cos(ky) \tag{5.11}$$

where $u = \bar{u}(x,t)$ is a dynamically evolving solution of

$$u_t + [f(u)]_x = -\partial_x\left(u^3\partial_x^3 u\right). \tag{5.12}$$

Substitution of (5.11) into (2.3) and neglecting terms of $O(\varepsilon^2)$ and higher yields

$$h_t = -[hf'(\bar{u})]_x - \partial_x(\bar{u}^3\partial_x^3 h + 3h\bar{u}^2\partial_x^3\bar{u}) + k^2[\partial_x(\bar{u}^3\partial_x h) + \bar{u}^3(\partial_x^2 h)] - k^4\bar{u}^3 h = \mathcal{L}_k h. \tag{5.13}$$

We numerically solve (5.12) for $\bar{u}$ and consequently find $h(x,t;k)$ from (5.13). For the numerical simulations included here we use an exponentially localised initial condition for $h(x,t;k)$ as described earlier (non-localised perturbations play a role later). We show examples of solutions generated by this numerical procedure in Figure 1 (left) and Figure 2 (left) (also see the later figures). In regions of the solution where the base state is locally constant, equation (5.13) reduces, in the limit of small k, to the simple convection-diffusion equation

$$h_t + f'(\bar{u})h_x = -\bar{u}^3\partial_x^4 h. \tag{5.14}$$

Therefore, away from the shock, perturbations with small wavenumber travel with the characteristic speed of the underlying $\bar{u}$-profile, $f'(\bar{u})$. For a compressive shock we have $f'(u_-) > 0 > f'(u_+)$ and this explains the movement of perturbations in Figure 1 (left), and also why the imposed perturbation catches the trailing compressive shock in

Figure 6. For undercompressive shocks, we have $0 > f'(u_-) > f'(u_+)$, so perturbations are always transported in the negative x direction (see Figure 2 (left)). Perturbations placed behind the undercompressive shock are thus swept away from the shock. In the eigenfunction analysis that follows, this is tantamount to requiring an exponentially growing eigenfunction as $x \to -\infty$ (see equation (5.20)). This is an undercompressive shock phenomena that does not occur for compressive shocks.

We pursue the eigenvalue problem by considering $\bar{u}(x,t) = \hat{u}(x)$ and looking for a solution of (5.13) of the separable form $h(x,t;k) = e^{\beta(k)t}\psi(x,k)$. This leads to the eigenvalue-eigenfunction relationship

$$\mathcal{L}_k\psi = \beta\psi. \tag{5.15}$$

where the operator $\mathcal{L}_k$ takes the form $\mathcal{L}_k = \mathcal{L}_0 + k^2\mathcal{L}_1 + k^4\mathcal{L}_2$, with

$$\begin{aligned} &\mathcal{L}_0\psi = -[\psi f'(\hat{u})]_x - \partial_x(\hat{u}^3\partial_x^3\psi + 3\psi\hat{u}^2\partial_x^3\hat{u}), \quad \mathcal{L}_1\psi = \partial_x(\hat{u}^3\partial_x\psi) + \hat{u}^3(\partial_x^2\psi), \\ &\mathcal{L}_2\psi = -\hat{u}^3\psi. \end{aligned} \tag{5.16}$$

In the small k limit, we can expand β and ψ as

$$\beta(k) = \beta_0 + k^2\beta_1 + O(k^4), \quad \psi(x,k) = \psi_0(x) + k^2\psi_1(x) + O(k^4). \tag{5.17}$$

For the choice $\beta_0 = 0$ with $\psi_0 = \hat{u}_x$ as a solution to $\mathcal{L}_0\psi_0 = \beta_0\psi_0$, we obtain the translational mode of (2.3) that arises due to the invariance of (2.3) to translations in x. For small k, therefore, whether solutions grow or decay for large time is dependent on the sign of β_1, which can be found from the solvability condition

$$\beta_1 \int_{-\infty}^{\infty} \hat{u}_x\pi_0 dx = \int_{-\infty}^{\infty} \pi_{0x}\hat{u}^3\hat{u}_{xx}dx + \int_{-\infty}^{\infty} \pi_0[f(\hat{u}) - f(u_+)]dx. \tag{5.18}$$

Here, $\pi_0(x)$ is the left eigenfunction that satisfies the formal adjoint of $\mathcal{L}_0$, and depends on the structure of the shock, i.e. whether it is compressive or undercompressive. This influences the growth rate of perturbation governed by β_1. In Figure 7 we plot $\log(||h||_\infty) = \log(\max_x\{h\})$ against t for $k = 0$, $k = 0.25$ and $k = 0.8$ for the compressive and undercompressive shocks shown in Figure 1 and Figure 2 respectively. The rapid change in $||h||_\infty$ at early times corresponds to the amplification of the perturbation by the shock front (see also [22]) and Figure 7 (left) also indicates the existence of the well known long-wave instability for compressive shock fronts. It is noteworthy that a similar long-wave instability does not occur for the undercompressive shock, as indicated in Figure 7 (right), and it is this absence which yields the stable front seen in the experiments.

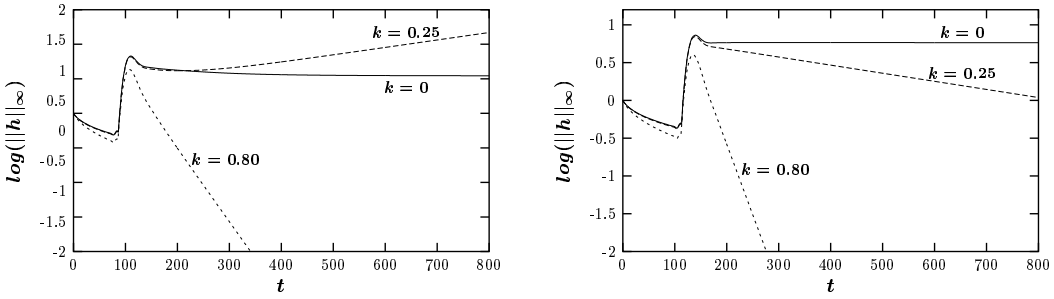

Fig. 7. (left) Transient growth for a perturbation interacting with a compressive shock. (right) Transient growth for a perturbation interacting with an undercompressive shock.

The work of [19] showed (by application of spectral theory) that, for compressive shocks, there exists a unique left eigenfunction given by the constant function $\pi_0 = 1/(u_+ - u_-)$ and (5.18) yields $\beta_1 = \int_{-\infty}^{\infty} \hat{u}(x)\,dx / \int_{-\infty}^{\infty} [f(\hat{u}) - f(u_+)]\,dx$. This consequently validates the previous compressive shock front stability analyses undertaken by [23] and [22].

We now turn our attention to double shock structures (featuring a leading undercompressive shock and a trailing compressive shock). We will show that a perturbation interacting with the undercompressive shock leads to non-local effects and consequently, the linear stability analysis of a single travelling wave is insufficient for describing the overall dynamics of a shock pair. We begin by explaining the mechanism for the transfer of information away from the undercompressive shock and then use this as a basis to investigate the subsequent interaction between the non-local perturbation and the trailing compressive shock. We find that the eigenfunction for undercompressive shocks grows exponentially in the far-field as $x \to -\infty$ and this exponential growth is, in fact, exactly that required to yield a translating wave which carries information away from the undercompressive shock; this is consistent with characteristics emanating from behind the undercompressive shock as described in Section 2. To understand the non-localised behaviour of the perturbation interacting with the undercompressive shock we employ a formal argument based on the structure of the eigenfunctions for small k. We consider (5.15) in the limit $x \to -\infty$ and look for solutions of the form $\psi(x) \sim e^{\mu x}$. The resulting quartic relationship for μ

$$\beta = -f'(u_-)\mu - u_-^3\mu^4 + 2k^2u_-^3\mu^2 - k^4u_-^3 \tag{5.19}$$

is valid for any k. For $\beta = 0$, $k = 0$, one of the roots of (5.19) is $\mu = 0$ corresponding to the translational mode. For small β, k, equation (5.19) coupled with (5.17) yields $\mu \sim -\beta_1/f'(u_-)$ where $f'(u_-) < 0$. So assuming we have stability in time, i.e. $\beta_1 < 0$ (as suggested by Figure 7 (right)), then $\mu < 0$, implying $\psi \sim e^{\mu x} \to \infty$ as $x \to -\infty$. In addition

$$h(x,t;k) \sim e^{k^2\beta_1 t}e^{-\beta_1 k^2/f'(u_-)} = e^{-\beta_1 k^2(x - f'(u_-))t/f'(u_-)} \qquad \text{as} \qquad x \to -\infty \tag{5.20}$$

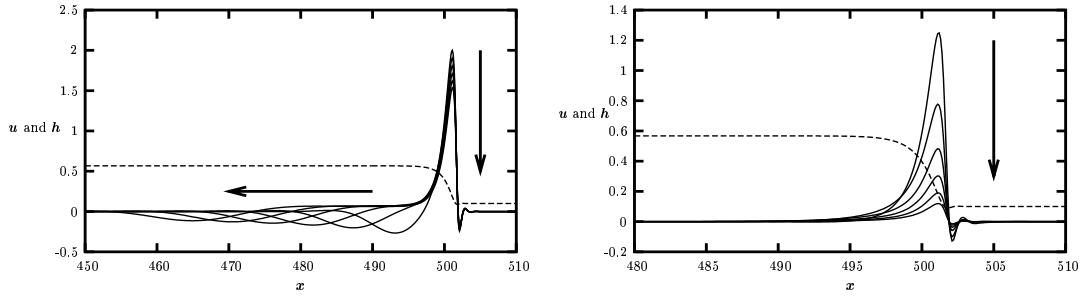

Fig. 8. Transient behaviour for a perturbation interacting with an undercompressive shock . The arrows indicate the direction of increasing time. (left) $k = 0.25$. (right) $k = 0.8$.

which is a translating wave with characteristic speed $f'(u_{-\infty})$. It is this non-local behaviour of the perturbation that leads to a transfer of information between undercompressive/compressive shock pairs (see Figure 8 (left) and Figure 10). We also note, from equation (5.19), that for large k, $\beta \sim -k^4 u_-^3 < 0$ as $x \to -\infty$. Therefore, the spatial and temporal scales (corresponding to μ and β respectively) are no longer coupled and any spatial phenomena as $x \to -\infty$ is rapidly damped by the exponentially decaying $e^{\beta t}$ term (see Figure 8 (right) for an illustration of this behaviour for $k = 0.8$). The far-field behaviour for undercompressive shocks should be contrasted to that for compressive shocks which have $\beta_1 > 0$ for small k (see Figure 7 (left)). The characteristic speed for compressive shocks is found to be negative for $u = u_-$, and so $\mu > 0$ as $x \to -\infty$; a similar analysis as $x \to \infty$ yields $\mu < 0$ [19]. Consequently, the eigenfunction ψ for compressive shocks decays exponentially in the far-field.

The form of $h(x, t; k)$ suggests rescaling the solution to (5.13) by $e^{\beta t}$ with the value of β taken from the data shown graphically in Figure 7 (right). We show such a rescaling for $k = 0.24$ and $\beta \approx -0.00098$ in Figure 9, where the undercompressive shock fronts have been shifted to coincide with one another. Solving for μ from (5.19) yields only one real, negative root, $\mu_* \approx -0.003377$. Figure 9 includes the curve of $Ae^{\mu_* x}$ with $A = 0.436$. There is good correspondence between the rescaled solutions and the calculated exponential growth rate as $x \to -\infty$. It is this far-field behaviour that we must use for matching into the compressive component of a double shock structure.

We show the interaction of the non-local perturbation with the trailing compressive shock in Figure 10; alternatively the compressive shock can be established independently and the exponential behaviour described above used to fix the right hand far-field boundary condition for the perturbation. The non-local perturbation interacts with the trailing shock and an initial amplification of the perturbation occurs (see Figure 10 (right)). The large transient growth of the perturbation excites nonlinearities in the full equation (2.3), and a backward-finger forms, as illustrated in Figure 4. The connection between the undercompressive and compressive shocks then allows a continual flux of mass into the compressive shock, until, at larger times, the size of the perturbation at the undercompressive shock becomes small with the transition layer between the two shocks becoming negligible. At this time, the linear stability dynamics correspond to a

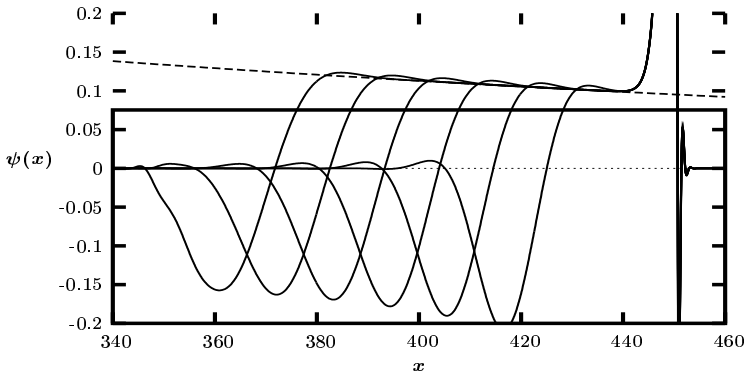

Fig. 9. Rescaled undercompressive shock solutions of (5.13) along with the curve $A\exp(\mu_* x)$ (dashed line). The parameters are $\mu_* \approx -0.003377$, $A = 0.436$, $k = 0.24$ and $\beta \approx -0.00098$. The solutions shown correspond to times $t = 500, 600, 700, 800, 900, 1000$.

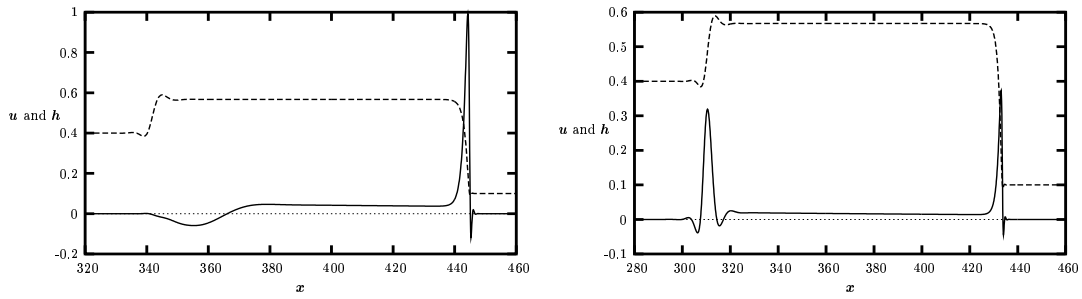

Fig. 10. Transient behaviour of shock pairs. (left) Non-local effects of the perturbation interacting with the undercompressive shock. (right) The perturbation connects the undercompressive and compressive shocks.

localised perturbation interacting with the trailing compressive shock. For a wavenumber of $k = 0.24$, analysis [19] and numerical simulations show that the large time growth rate of the perturbation is negative, so that the perturbation (and consequently the backward-finger) decays away. Choosing a wavenumber disturbance where $k < k_c \approx 0.17$ yields a perturbation that continues to grow for large time; similarly, the backward-finger continues to lengthen.

6 Conclusions

In this work, we have considered the propagation of information through the double shock structures that form under appropriate conditions for thin films that are driven by Marangoni stresses acting against gravity. By application of a lubrication approximation we derived an evolution equation (2.3) that models the experimentally observed behaviour extremely well as indicated by the close similarity between the experimental results and the two-dimensional numerical computations of (2.3); these results are also supported by the previous one-dimensional results from [9]. We have

considered mathematically the propagation of a perturbation, and have shown that the effects of a localised perturbation in front of the leading undercompressive shock lead to nonlocal effects at the trailing compressive shock.

The application of characteristic methods allows an investigation to be undertaken into the transfer of information between the two shocks. This approach consequently provides a clear interpretation of the interaction of perturbations with the shock pairs. The coupling of this theory with a numerical stability study of the time dependent base states then leads to a detailed understanding of the free surface phenomena.

The stability of the undercompressive shock as noted in previous papers (see [19] and references therein) and which is due, in part, to the exponentially growing eigenfunction as $x \to -\infty$, has an obvious applicability to many industrial coating processes where the stability of the coating front is of utmost importance. Although we have employed a combination of a Marangoni stress and gravity, we expect that similar results can be obtained for other opposing body forces, such as the centripetal force arising in spin coating processes. It is also a relatively simple matter to extend the stability study undertaken in this paper to more complicated problems involving several timescales and complex spatial structures including multiple shocks, rarefaction fans and various other profile discontinuities. The work in this paper therefore provides a basis on which to build detailed investigations of various complex free surface phenomena relevant to the coatings industry.

Acknowledgements

We thank Tom Witelski for useful discussions. This work is supported by NSF grants DMS-0074049, DMS-0244498, and ACI-0321917, and ONR grants N000140110290 and N000140410078. MB also acknowledges the support of an EPSRC postdoctoral fellowship.

References

[1] H. Huppert, Flow and instability of a viscous current down a slope, Nature 300 (1982) 427–429.

[2] A. M. Cazabat, F. Heslot, S. M. Troian, P. Carles, Fingering instability of thin spreading films driven by temperature gradients, Nature 346 (6287) (1990) 824–826.

[3] D. E. Kataoka, S. M. Troian, Stabilizing the advancing front of thermally driven climbing films, J. Coll. Int. Sci. 203 (1998) 335–344.

[4] D. E. Kataoka, S. M. Troian, A theoretical study of instabilities at the advancing front of thermally driven coating films, J. Coll. Int. Sci. 192 (1997) 350–362.

[5] M. A. Spaid, G. M. Homsy, Stability of Newtonian and viscoelastic dynamic contact angles, Phys. Fluids 8 (1996) 460–478.

[6] M. H. Eres, L. W. Schwartz, R. V. Roy, Fingering phenomena for driven coating films, Phys. Fluids 12 (2000) 1278–1295.

[7] X. Fanton, Etalement et instabilités de films de mouillage en presence de gradients de tension superficielle, Ph.D. thesis, Université Paris 6 Pierre et Marie Curie, Paris (1998).

[8] A. L. Bertozzi, A. Münch, X. Fanton, A. M. Cazabat, Contact line stability and 'undercompressive shocks' in driven thin film flow, Phys. Rev. Lett. 81 (23) (1998) 5169–5172.

[9] A. L. Bertozzi, A. Münch, M. Shearer, Undercompressive shocks in thin film flows, Physica D 134 (4) (1999) 431–464.

[10] J. Sur, A. L. Bertozzi, R. P. Behringer, Reverse undercompressive shock structures in driven thin film flow, Phys. Rev. Lett. 90 (12) (2003) 126105.

[11] A. Münch, Pinch-off transition in Marangoni-driven thin films, Phys. Rev. Lett. 91 (2003) 016105.

[12] A. Münch, Shock transitions in Marangoni-gravity driven thin film flow, Nonlinearity 13 (2000) 731–746.

[13] X. Fanton, A. M. Cazabat, D. Quéré, Thickness and shape of films driven by a Marangoni flow, Langmuir 12 (24) (1996) 5875–5880.

[14] J. Ockendon, S. Howison, A. Lacey, A. Movchan, Applied partial differential equations, Oxford University Press, 2003.

[15] A. Münch, A. L. Bertozzi, Rarefaction-undercompressive fronts in driven films, Phys. Fluids 11 (10) (1999) 2812–2814.

[16] J. Sur, T. P. Witelski, R. P. Behringer, Steady-profile fingering flows in Marangoni driven thin films, submitted to Phys. Rev. Lett.

[17] T. P. Witelski, M. Bowen, ADI schemes for higher-order nonlinear diffusion equations, Appl. Num. Math. 45 (2-3) (2003) 331–351.

[18] A. L. Bertozzi, M. Bowen, Thin film dynamics: theory and applications, in: A. Bourlioux, M. J. Gander (Eds.), Modern Methods in Scientific Computing and Applications, Vol. 75 of NATO Science Series II, Kluwer Academic Publishers, 2001, pp. 31–79, Proceedings of the NATO Adv. Study Institute, Montreal Canada, 2001.

[19] A. Bertozzi, A. Münch, M. Shearer, K. Zumbrun, Stability of compressive and undercompressive thin film travelling waves, Euro. J. Appl. Math. 12 (3) (2001) 253–291.

[20] O. Matar, S. M. Troian, Spreading of a surfactant monolayer on a thin liquid film: Onset and evolution of digitated structures, Chaos 9 (1).

[21] M. R. E. Warner, R. V. Craster, O. K. Matar, Unstable van der Waals driven line rupture in Marangoni driven thin viscous films, Phys. Fluids 14 (5) (2002) 1642–1654.

[22] A. L. Bertozzi, M. P. Brenner, Linear stability and transient growth in driven contact lines, Phys. Fluids 9 (3) (1997) 530–539.

[23] S. M. Troian, E. Herbolzheimer, S. A. Safran, J. F. Joanny, Fingering instabilities of driven spreading films, Europhys. Lett. 10 (1) (1989) 25–30.